UC Berkeley
UC Berkeley Previously Published Works

Title

The impact of the 2015/2016 El Niño on global photosynthesis using satellite remote sensing

Permalink
https://escholarship.org/uc/item/6zj0672f

Journal
Philosophical Transactions of the Royal Society B Biological Sciences, 373(1760)

ISSN
0962-8436

Authors
Luo, Xiangzhong
Keenan, Trevor F
Fisher, Joshua B
et al.

Publication Date
2018-11-19

DOI
10.1098/rstb.2017.0409

Copyright Information
This work is made available under the terms of a Creative Commons Attribution-NonCommercial-ShareAlike License, available at https://creativecommons.org/licenses/by-nc-sa/4.0/

Peer reviewed

eScholarship.org Powered by the California Digital Library
University of California

***Phil. Trans. R. Soc. B.* article**

PHILOSOPHICAL TRANSACTIONS B

Phil. Trans. R. Soc. B.
doi:10.1098/not yet assigned

The impact of the 2015-2016 El Niño on global photosynthesis using satellite remote sensing

Xiangzhong Luo [1,2*], Trevor F. Keenan [1,2*], Joshua B. Fisher [3], Juan-Carlos Jiménez [4], Jing M. Chen [5], Chongya Jiang [6], Weimin Ju [7], Naga-Vineet Perakalapudi [3], Youngryel Ryu [6,8], Jovan M. Tadić [1]

1. Climate and Ecosystem Sciences Division, Lawrence Berkeley National Laboratory, Berkeley, CA, USA.
2. Department of Environmental Science, Policy and Management, University of California, Berkeley, CA, USA.
3. Jet Propulsion Laboratory, California Institute of Technology, Pasadena, CA, USA.
4. Global Change Unit, Image Processing Laboratory, University of Valencia, Valencia, Spain.
5. Department of Geography and Planning, University of Toronto, Toronto, ON, Canada.
6. BK 21 Plus Team, Seoul National University, Republic of Korea
7. International Institute for Earth System Science, Nanjing University, China.
8. Department of Landscape Architecture and Rural Systems Engineering, Seoul National University, Republic of Korea

Keywords: ENSO, Gross Primary Productivity, solar-induced fluorescence

*Author for correspondence (xzluo@lbl.gov; trevorkeenan@lbl.gov).

Summary

The El Niño-Southern Oscillation exerts a large influence on global climate regimes and on the global carbon cycle. Although El Niño is known to be associated with a reduction of the global total land carbon sink, results based on prognostic models or measurements disagree over the relative contribution of photosynthesis to the reduced sink. Here, we provide an independent remote sensing based analysis on the impact of the 2015-2016 El Niño on global photosynthesis using six global satellite-based photosynthesis products and a global solar-induced fluorescence (SIF) dataset.

An ensemble of satellite-based photosynthesis products showed a negative anomaly of -0.7 ± 1.2 PgC in 2015, but a slight positive anomaly of 0.05 ± 0.89 PgC in 2016, which when combined with observations of the growth rate of atmospheric carbon dioxide concentrations suggests that the reduction of the land residual sink was likely dominated by photosynthesis in 2015 but by respiration in 2016. The six satellite-based products unanimously identified a major photosynthesis reduction of -1.1 ± 0.52 PgC from savannas in 2015 and 2016, followed by a highly uncertain reduction of -0.22 ± 0.98 PgC from rainforests. Vegetation in the Northern Hemisphere enhanced photosynthesis before and after the peak El Niño, especially in grasslands (0.33 ± 0.13 PgC). The patterns of satellite-based photosynthesis ensemble mean were corroborated by SIF, except in rainforests and South America, where the anomalies of satellite-based photosynthesis products also diverged the most. We found the inter-model variation of photosynthesis estimates was strongly related to the discrepancy between moisture forcings for models. These results highlight the importance of considering multiple photosynthesis proxies when assessing responses to climatic anomalies.

Introduction

The biosphere of the earth currently functions as a net carbon sink that offsets around 30% of anthropogenic CO_2 emissions [1]. The ability to predict carbon sink dynamics is thus essential to understanding the future evolution of a changing climate. Multiple streams of evidence from atmospheric CO_2 observations [2], ground biomass measurements [3,4], remote sensing [5,6] and Dynamic Global Vegetation Models (DGVMs) [1,7] unanimously suggest the terrestrial carbon sink has been increasing thanks to the effect of elevated CO_2 [7,8] and prolonged vegetation growing seasons [9], meanwhile, their estimates of year-to-year variation of the terrestrial carbon sink differ markedly [10]. Since the land-atmosphere CO_2 flux in tropics contributes the majority of the variability in the terrestrial carbon cycle [11–13], El Niño-South Oscillation (ENSO), a key mode that alternates the tropical climate between dry and wet states, provides a critical opportunity to study carbon cycle variability. El Niño impacts the tropical terrestrial carbon cycle through temperature [14] , droughts [15], fires [16] and tree mortality [17]. In addition, El Niño influences the global climate and places a large constraint on the carbon cycle of extratropical regions through teleconnections [18,19].

In the El Niño phase, tropical regions experience anomalously high temperatures and low precipitation. High temperatures can either suppress photosynthesis [20] or enhance respiration [21] to reduce the terrestrial carbon sink, while changes in hydroclimate can affect the local sensitivities of photosynthesis and respiration to temperature [22,23]. Though it is known that El Niño is linked to reduced net ecosystem productivity (NEP), attribution to specific carbon processes responsible remains challenging [24], particularly in terms of the relative contribution of changes in gross primary productivity (GPP), ecosystem respiration (Reco), autotrophic respiration of vegetation (Ra), heterotrophic respiration (Rh) and net primary productivity (NPP) (NEP = GPP - Reco = GPP - Ra - Rh = NPP – Rh).

At the global scale, Jones et al. [25] used a general circulation model HadCM3LC to find that El Niño reduced NEP by 1.8 Pg yr^{-1} per °C rise in the tropical Pacific sea surface temperature, and GPP, Ra and Rh contributed 33%, 25% and 42% to the decrease, respectively. In comparison, Cavaleri et al. [26] reported that GPP, Ra and Rh contributed 55%, 11% and 34% to the NEP reduction in a tropical forest during the 1997-1998 El Niño, using multiple ground-based measurements. Some studies running a prognostic DGVM VEgetation-Global-Atmosphere-Soil (VEGAS) reported a NEP decrease of 4 Pg yr^{-1} in the tropics during El Niño [11], where NPP and Rh accounted for 68-75% and 25-32% of the decrease, respectively [11,27]. A recent study reported that El Niño not only reduced GPP in tropics but also enhanced GPP in temperate regions of South and North America, through analyzing the teleconnection between an ensemble of GPP of nine DGVMs and ENSO [18]. The ENSO - carbon response is also dependent on the distinct characteristics of each El Niño. For example, a recent study using the DGVM VEGAS and atmospheric inversions suggested that decreased GPP dominated the NEP reduction during the 1997-1998 El Niño, but increased Reco dominated in 2015-2016; in 2015-2016, GPP of tropical Africa was reported to have increased and compensated the decrease of GPP over other tropical regions [28].

While many studies rely on DGVMs and their ensemble to study the impact of El Niño, remote sensing (RS) based proxies of GPP provide a potential independent constraint for impact assessment. RS indices, including Normalized Difference Vegetation Index (NDVI) and Enhanced Vegetation Index (EVI), and RS derived biophysical variables, including Leaf Area Index (LAI) and fraction of Absorbed Photosynthetic Active Radiation (fAPAR), have been extensively used to estimate NPP and GPP [7,29,30]. Some studies have looked into the relationship between ENSO and satellite-based photosynthesis. Hashimoto et al. [31] found the interannual variability of NPP derived from an AVHRR light use efficiency (LUE) model was significantly related to ENSO during 1982 to 1999, particularly at low latitudes. Gonsamo et al. [19] further reported that ENSO strongly influenced NPP anomalies at the continental scale but exerted a weak control at the global scale, using a 30 years NDVI sequence as a proxy for NPP, while Ballantyne et al. [32] examined MODIS GPP and found that high temperatures in El Niño years were more likely to enhance global Rh while GPP was relatively unaffected. Each of these studies, however, derived their conclusions from only one GPP proxy, without considering how results were influenced by proxy choice.

Solar-induced Fluorescence (SIF) are photons in the wavelength around 660 nm to 800 nm that are emitted through the de-excitation of excited leaf chlorophyll molecules, which are simultaneously responsible for providing energy to photosynthesis [33]. SIF has spurred intense interest in the carbon research community in recent years, since several groups have found significant correlations between satellite-measured SIF and ground based estimates of GPP [34,35]. SIF is therefore regarded as another benchmark to evaluate the variability of terrestrial GPP. Currently, multiple global SIF observations are available, including the Global Ozone Monitoring-2 (GOME-2) sensor onboard the Meteorological Operational Satellites MetOp-A and MetOp-B, the Greenhouse Gases Observing Satellite (GOSAT) and the Orbiting Carbon Observatory-2 (OCO-2). Some groups have exploited SIF for El Niño studies: Liu et al. [24] employed GOSAT SIF along with column CO_2 fraction observed by GOSAT and OCO2 in tropical forests to find that the 2015-2016 El Niño reduced NEP in spatially different ways: the NEP reductions in Amazon, tropical Africa and tropical Asia were driven by decreased GPP, increased Reco and wild fires, respectively. A recent study found Amazon ecosystems experienced a 8.2% decrease in photosynthesis during the drought of 2015-2016 El Niño, using GOME-2 SIF as an indicator for photosynthesis [36], though a later study suggested the SIF decrease is an artefact [37]. As a direct proxy of photosynthesis, SIF products can provide new understanding in respect to the impacts of El Niño at various scales.

Here, we assess the impact of the 2015-2016 El Niño event on global photosynthesis using a suite of six different RS GPP products and four SIF datasets. Using an ensemble of RS GPP products can minimize the inherent uncertainty associated with an individual model which may or may not be an outlier of a community of models. The 2015-2016 El Niño was one of the strongest El Niño events on record since the late 20th century, with extreme heat and drought being reported in many tropical regions [38,39]. It lasted around 15 months from March 2015 to May 2016, with the peak appeared around October 2015 to February 2016 [40]. It provides a rare window where multiple satellite observations and RS GPP products overlapped with an El Niño event.

Materials and Methods

1. The MODerate Resolution Imaging Spectroradiometer (MODIS) GPP products (Collection 55 and 6)

The MODIS GPP product is the first operational, near-real-time estimate of GPP for the vegetated land surface. It adopts the light use efficiency (LUE) theory proposed by Monteith [41,42] to calculate GPP as a product of absorbed photosynthetic radiation (APAR) and a conversion efficiency, ε:

$$GPP = \varepsilon \times APAR = \varepsilon \times fAPAR \times PAR$$

where ε is prescribed using a biome-specific lookup table and constrained by air temperature and vapor pressure deficit for suboptimal climatic conditions [43]. PAR is photosynthetic active radiation, and fAPAR is the fraction of absorbed PAR derived from MODIS NDVI.

The Numerical Terradynamic Simulation Group (NTSG) at the University of Montana provides a version of MODIS GPP (MOD17 collection 55) for ecological studies, which rectifies the underestimation of GPP incurred by cloud-contaminated fAPAR pixels in the near-real-time MODIS GPP product (MOD17 collection 5) [29]. NTSG uses NCEP Reanalysis II (http://www.ntsg.umt.edu/project/modis/mod17.php) to drive the GPP algorithm and has been updated to 2015. This product is denoted as MODIS-c55 in this study. It is provided at a monthly step and 0.5° resolution.

We also used a new release of MODIS GPP (MOD17 collection 6) from 2001 to 2016, with an original resolution of 500 m and a time interval of 8 days. We upscaled the product to 0.5° resolution and a monthly step. This product is denoted as MODIS-c6 in this study. PAR and other surface meteorological variables provided by the Global Modeling and Assimilation Office (GMAO) are used to simulate MODIS-c6 GPP. The MODIS-c6 GPP was generally 5-10 PgC yr^{-1} smaller than the MODIS-c55 GPP, which was also noted in Zhang et al. [44]. The direct effect of CO_2 fertilization on ε is not considered in MODIS-c55 and MODIS-c6 [45].

In order to extend the MODIS-c55 GPP to 2016, we used a simple ratio method to extrapolate 2016 MODIS-c6 GPP into 2016 MODIS-c55 GPP pixel by pixel. The ratio for each pixel was acquired based on the 2015 MODIS-c55 and MODIS-c6 GPP, assuming the systematic difference between the GPP of MODIS-c55 and MODIS-c6 in 2016 resembled that in 2015 the most. This method can cause an uncertainty of 1.6 PgC for the extrapolated 2016 MODIS-c55 GPP if choosing a different year to calculate the ratios.

2. Vegetation Photosynthesis Model (VPM)

Similar to the MODIS GPP model, the VPM model is developed based on LUE theory [46]. The VPM model updates the biome-specific lookup table used by the MODIS model and uses EVI as a proxy to calculate fAPAR, in an attempt to account for the effect of leaf chlorophyll rather than just leaf quantity [46]. Like most LUE-based models, VPM does not explicitly consider the effect CO_2

fertilization in the model [45]. VPM uses air temperature from the NCEP Reanalysis II [44] gridded meteorological dataset and a satellite derived Land Surface Water Index (LSWI) [47] to constrain ε. VPM GPP is available from 1980 to 2016 at 0.5° and a monthly resolution.

3. Breathing Earth System Simulator (BESS)

BESS is a satellite-driven diagnostic model built on the enzyme kinetic framework designed by Farquhar et al. [48], to estimate global GPP and evapotranspiration [49,50]. BESS integrates algorithms for atmospheric radiative transfer, two-leaf canopy radiative transfer, photosynthesis and surface energy balance with a wide range of MODIS products, including physical variables (i.e. MODIS aerosol, cloud, atmospheric profile and land surface temperature (LST)) and biophysical variables (i.e. LAI and clumping index). BESS considers the effect of CO_2 fertilization by using spatially and temporally varying atmospheric CO_2 in the model. In this study, the BESS model used air temperature acquired from ERA Interim (ERAI). Two snapshot estimates (Terra and Aqua) of GPP were upscaled to daily sums using a simple cosine function [51]. We used the BESS GPP products from 2000 to 2016 at a monthly and 0.5° resolution (http://environment.snu.ac.kr/bess_flux/).

4. Photosynthesis-respiration model (PR model)

The PR model is a LUE model developed from first principles of photosynthetic theory [52]. It applies the least cost and the coordination hypotheses to convert the popular biochemical photosynthesis model [48] into a LUE form [7,53]. The effect of CO_2 fertilization on GPP is explicitly considered in the PR model. In this study, the PR model uses fAPAR derived from AVHRR 3rd generation NDVI by Global Inventory Modeling and Mapping Studies (GIMMS) [54], following Keenan et al. [7]. The meteorological forcings for the PR model, including total photosynthetic active radiation, air temperature and water vapor potential, were provided by the Climate Research Unit (CRU) at a monthly and 0.5° resolution [55].

5. Boreal Ecosystem Productivity Simulator (BEPS)

BEPS is a terrestrial biosphere model built on the enzyme kinetic framework designed by Farquhar et al. [48], to estimate global carbon fluxes and evapotranspiration [56,57]. BEPS integrates algorithms for two-leaf canopy radiative transfer, photosynthesis, surface energy balance and soil water regime with satellite-derived biophysical variables (i.e. LAI and clumping index) [58]. The effect of CO_2 fertilization on GPP is explicitly considered in BEPS. In this study, we used a version of BEPS run at daily step [56]. The meteorological forcings for the BEPS model are daily maximum temperature, minimum temperature, precipitation, radiation and relative humidity acquired from CRU-NCEP. We used the BESS GPP estimation from 2000 to 2016 at a monthly and 0.5° resolution.

6. Solar-induced fluorescence

We used four SIF datasets in this study, namely, GOME-2 onboard MetOp-A (GOMEA) and onboard MetOp-B (GOMEB), GOSAT and OCO2. GOMEA ranges from 01/2007 to 12/2016, GOMEB ranges from 03/2013 to 12/2016, GOSAT ranges from 04/2009 to 05/2016 and OCO2 ranges from 09/2014 to 12/2016. OCO2 SIF was processed from OCO2_L2_Lite_SIF (V8r) and GOSAT SIF was processed from ACOS_L2_Lite_FP (V7.3). Monthly SIF 0.5° gridded data were generated by averaging observations in its latitude and latitude bounds for each 0.5° pixel for both OCO2 and GOSAT. All flags were applied before processing the gridded data for quality control. GOMEA and GOMEB SIF was processed from GOME-2 version 2 (V27) 740 nm terrestrial chlorophyll fluorescence data from MetOp-A and MetOp-B. Its monthly SIF data products were then generated by cropping land area and pixel values were capped between 0-3 mW m^{-2} nm^{-1} sr^{-1} for quality control.

7. Gridded meteorological datasets

RS GPP models were driven by gridded meteorological datasets of different types, including CRU, NCEP Reanalysis II and ERAI. Along with these datasets, we also assessed the temperature and precipitation records from CRU-NCEP, the Modern-Era Retrospective analysis for Research and Applications (Version 2; MERRA2), and the Tropical Rainfall Measuring Mission (TRMM), to support an attribution analysis of the potential difference between RS GPP estimates. Among these gridded datasets, NCEP, ERAI, MERRA2 are reanalysis, CRU is based on in-situ observations, TRMM is a remote sensing product, and CRU-NCEP is a combination of reanalysis and observations. ERAI and CRU were downloaded at 0.5°; TRMM was at 0.25 x 0.25° and we downscaled it using average values within each 0.5° cell; MERRA2 was at around 0.5° x 0.6° and was converted to 0.5° x 0.5° using nearest neighbor interpolation. NCEP and CRU-NCEP were interpolated from 1.875° x 1.875° to 0.5° x 0.5° using linear interpolation. All meteorological datasets are temporally aggregated to the monthly step.

8. Plant Functional Types

In order to explore the ecoregion-specific response to El Niño, we used the plant functional types (PFTs) classified by the MODIS Land Cover maps [59] curated at 0.5°. For each 0.5° grid cell, we used the PFT that was most prevalent during the period 2000–2012. The acronyms for PFTs used in this study are EBF (evergreen broadleaf forest), DF (deciduous broadleaf forest and deciduous needleleaf forest), ENF (evergreen needleleaf forest), MF (mixed forest), CRO (cropland), SAV (savanna and woody savanna), GRA (grassland), SH (closed shrubland and open shrubland) and WET (wetland).

9. Global Carbon Budget

We used global carbon budget data from the Global Carbon Project [1] to quantify the total carbon sink reductions in 2015 and 2016. The Global Carbon Project data set is a compilation of estimates of all major components of the global carbon budget, based on the combination of observations, statistics and model estimates. In this study, NEP was estimated from the residual of fossil fuel emission, land use change, atmospheric CO_2 growth and the ocean sink.

10. Statistical Analysis

Anomalies of RS GPP and SIF were calculated using the mean GPP or SIF of the available years of each dataset as the baseline, except for the OCO2 SIF which only has two years of record. We further detrended each dataset to remove the effects of factors other than climate (i.e. CO_2 fertilization and growing season changes) on carbon uptake, using background linear trend of the dataset as the baseline. Detrended SIF also removed the artefact degradation in SIF signals from GOME-2 [37]. Note that the detrended anomaly is relative to the linear trend, and therefore is sensitive to the period chosen to define the trend. Here we used all available records (< 18 years) of each product to quantify its respective linear trend, but acknowledge that the use of a longer timescale could potentially affect the results. In addition, using an ensemble of RS GPP products allows for the quantification of uncertainties and identification of mean behavior of RS products.

We used one-tailed student's t test to quantify the significance of GPP changes during the El Niño event, by detecting whether the ensemble of detrended RS GPP anomalies (n=6) is statistically larger or smaller than 0 ($p < 0.05$). If the null hypothesis is rejected, then we regard the model ensemble identifies a significant GPP anomaly, and the members of the ensemble are consistent with each other because their anomalies are likely in one direction. Based on the detrended anomalies of GPP and SIF, we further calculated the Z score for each product using the equation: $z = (x - \mu) / \sigma$, where x is a variable, μ and σ are the mean and the standard deviation of the variable. We used the Z score to evaluate the consistency and inconsistency between models.

Results

1. The Impact of El Niño on global GPP

In order to assess the extent of the response in an individual time period, it is necessary to characterize background variability and baseline GPP. All RS GPP products except MODIS-c55 demonstrated continuously increasing trends from 2000 to 2016 ($p < 0.05$) (Figure 1a). The slopes of the trends were 0.41 ± 0.11, 0.48 ± 0.16, 0.62 ± 0.10, 0.06 ± 0.09, 0.30 ± 0.13 and 0.41 ± 0.09 PgC yr^{-2} for the PR model, BESS, BEPS, MODIS-c55, MODIS-c6 and VPM, respectively. Meanwhile, GOMEA and GOMEB SIF showed negative trends, due to a known issue of the degradation of instrument onboard the GOME-2 [60]. GOSAT SIF did not show a statistically significant trend during 2007 to 2015. OCO2 has been operating for a short period since late 2014, but it captured an increase in global SIF from 2015 to 2016 (Figure 1a).

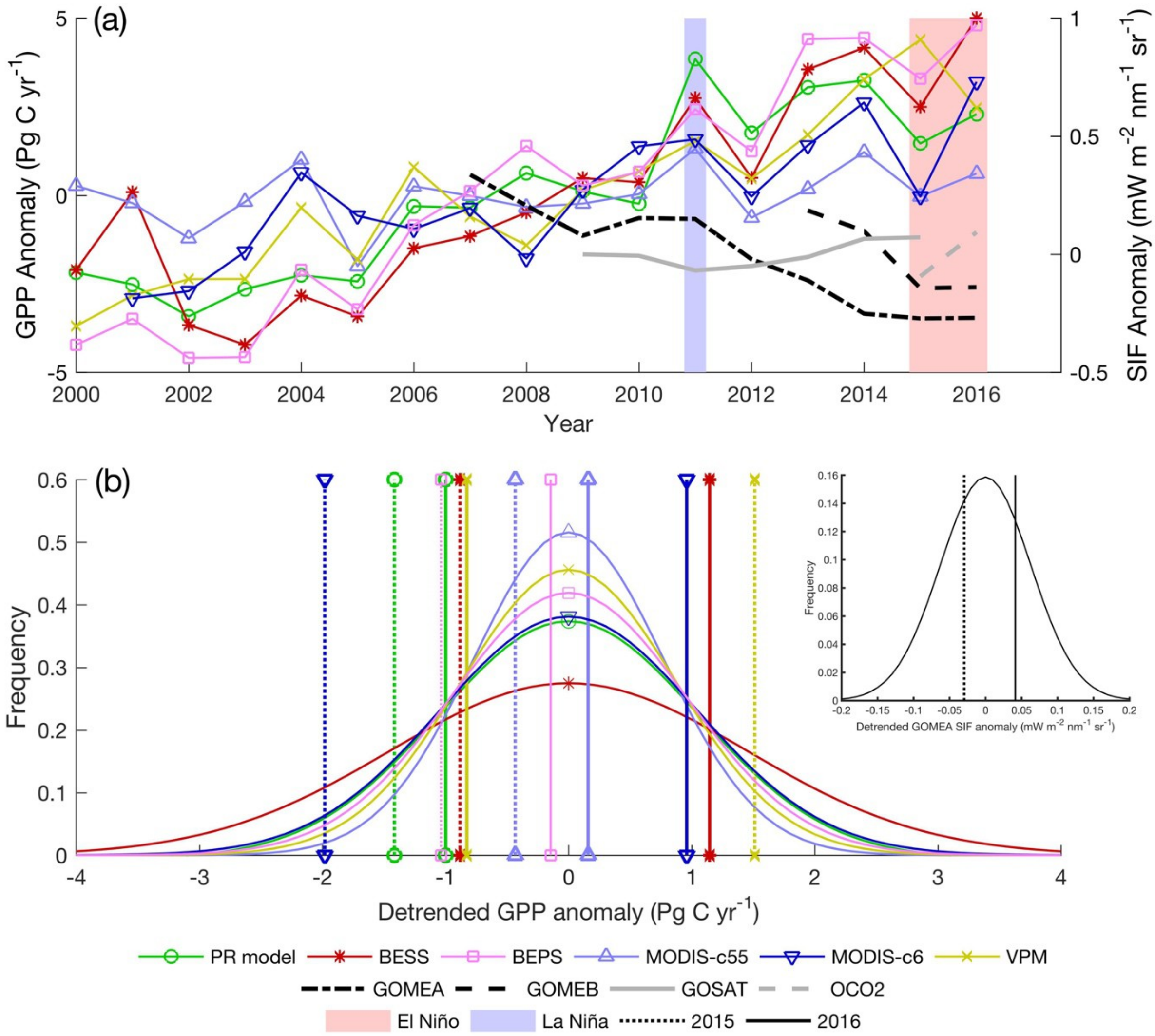

Figure 1. (a) The RS GPP and SIF anomalies from 2000 to 2016, relative to the time-average baseline GPP or SIF, for six RS GPP products and four SIF products; (b) The variability of detrended RS anomalies from 2000 to 2016, using the linear trend of RS GPP as the baselines. The anomalies of the two El Niño years 2015 and 2016 are labelled by vertical lines of different styles. The inset indicates the long-term variability of detrended GOMEA SIF, and the detrended anomalies of GOMEA SIF in 2015 and 2016.

To explore the impact of El Niño on GPP, we detrended the annual GPP to remove the impact of CO_2 fertilization, lengthening growing seasons and the long-term climate trend. The six RS GPP products displayed different magnitudes of background variability (Figure 1b): the standard deviation of detrended GPP anomalies from the largest to the smallest was 1.41 PgC yr^{-1} for BESS, 1.02 PgC yr^{-1} for the PR model, 1.01 PgC yr^{-1} for MODIS-c6, 0.95 PgC yr^{-1} for BEPS, 0.75 PgC yr^{-1} for MODIS-c55 and 0.85 PgC yr^{-1} for VPM. GOMEA SIF, the only long-term SIF product available during El Niño, had a background variability of 0.063 mW m^{-2} nm^{-1} sr^{-1}. The detrended GPP anomalies of the six RS products and the detrended SIF anomaly of GOMEA followed a Gaussian distribution ($p < 0.05$, Shapiro-Wilk test [61]).

We found large discrepancies between model estimates on the global impact of El Niño at the annual scale (Figure 1b; Figure S1). In 2015, the detrended GPP anomalies from different models ranged between -1.98 and -0.43 PgC, with the exception of the VPM model which showed a strong positive detrended anomaly of 1.51 PgC. In 2015, the model ensemble was -0.7 ± 1.2 PgC. In 2016, GPP estimated from different models distributed in a wider range from – 1.00 to 1.15 PgC, with the ensemble mean of 0.05 ± 0.89 PgC. In 2016, The PR model and the VPM model showed negative detrended GPP anomalies, BESS and MODIS-c6 showed positive anomalies and BEPS and MODIS-c55 showed almost neutral anomalies (Figure 1b).

To put our calculation of GPP anomalies into the context of global carbon cycle, we calculated the anomalies of NEP as the residual of anthropogenic emissions, atmospheric growth and ocean sink [1] and detrended the NEP anomalies from 2000 to 2016 to remove the long-term trend of increasing uptake. In 2015 and 2016, the detrended NEP anomalies were -1.16 ± 0.47 PgC and -1.38 ± 0.87 PgC, respectively (Figure S2). Using the ensemble mean of detrended GPP and NEP anomalies, we found that the GPP accounted for 60% of the NEP reduction in 2015, but made no contribution to the NEP reduction in 2016. This implies that an increase in Reco and biomass burning likely dominated the reduction in the carbon sink in 2016.

2. Regional distribution of GPP anomalies in the El Niño years

Although the detrended anomalies of the RS GPP products differed at the global scale, significant anomalies were evident using the ensemble of GPP products at some regions (Figure 2). The ensemble of RS GPP identified significant changes in photosynthesis (one-tailed t-test, $p < 0.05$) over 53% and 52% of the vegetated land surface in 2015 and 2016, respectively (Figure 2 c-d). The RS GPP ensemble mean identified significant photosynthesis changes over large areas in the southern Africa, Australia, temperate Eurasia and North America and small parts of the eastern Amazon. Meanwhile, the ensemble of RS GPP products cannot provide reliable estimates over some key carbon sink regions such as the rainforests in west Amazon and tropical Asia. If we only consider the pixels that show significant GPP anomalies, the ensemble means of global GPP detrended anomaly were -0.76 ± 0.45 and 0.51 ± 0.61 PgC in 2015 and 2016, respectively, compared to -0.7 ± 1.2 and 0.05 ± 0.89 PgC when considering all regions.

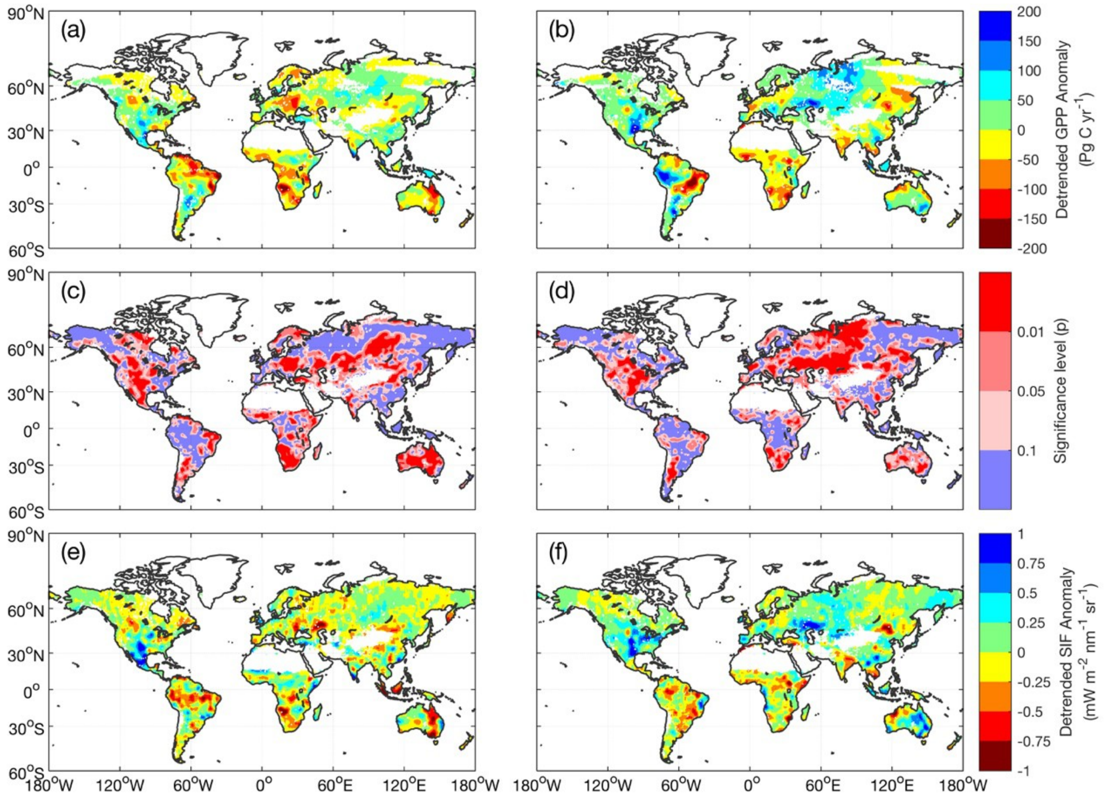

Figure 2. (a-b) Mean detrended GPP anomalies (g C m^{-2} yr^{-1}) from the ensemble of RS models in 2015 (a) and 2016 (b), usig the linear trends of RS GPP from 2000 to 2016 as the baselines. Only the pixels where all six RS products have values are shown; (c-d) significance level of the consistency between members of the RS GPP ensemble; (e-f) Detrended SIF anomalies from GOMEA in 2015 (e) and 2016 (f), using the linear trend of GOMEA SIF from 2007 to 2016 as the baseline.

The map of GOMEA SIF anomalies identified hotspots of GPP anomalies that are similar to the ensemble mean of RS estimates (Figure 2). Both SIF and the ensemble mean of RS estimates indicated that southern Africa, eastern Australia and central Europe in 2015 and western Australia, India and central Africa in 2016 experienced reductions in photosynthesis. However, for some regions, such as tropical America, SIF demonstrated a rather different landscape of anomaly than the RS ensemble mean. Overall, the global distribution of SIF detrended anomalies (Figure 2 e-f) was significantly correlated to the detrended anomalies of GPP ensemble, with spatial correlation coefficients of 0.26 and 0.27 in 2015 and 2016 ($p < 0.05$), respectively.

At the regional scale, our results showed marked GPP reductions in Africa and savannas (SAV) during the 2015-2016 El Niño, which was unanimously supported by all RS models and SIF (Figure 3). In 2015, all continents except North America and Asia showed negative GPP anomalies. With the evolution of the El Niño event, global photosynthesis increased in 2016 except a persistent large drop in Africa. The total GPP decrease contributed by Africa was around -1.24 ± 0.33 PgC, more than double of South America GPP decrease (-0.55 ± 0.72 PgC). In both years of El Niño, we found that majority of GPP decrease came from savannas, whose contribution (-1.1 ± 0.52 PgC) surpassed the highly uncertain GPP reduction of evergreen broadleaf forests (EBF) (-0.22 ± 0.98 PgC). Meanwhile, GPP of grasslands (GRA) and croplands (CRO) increased considerably by 0.33 ± 0.13 PgC and 0.14 ± 0.17 PgC in 2015-2016. PFTs other than SAV, EBF, GRA and CRO showed almost neutral changes in GPP during the El Niño event (Figure 3).

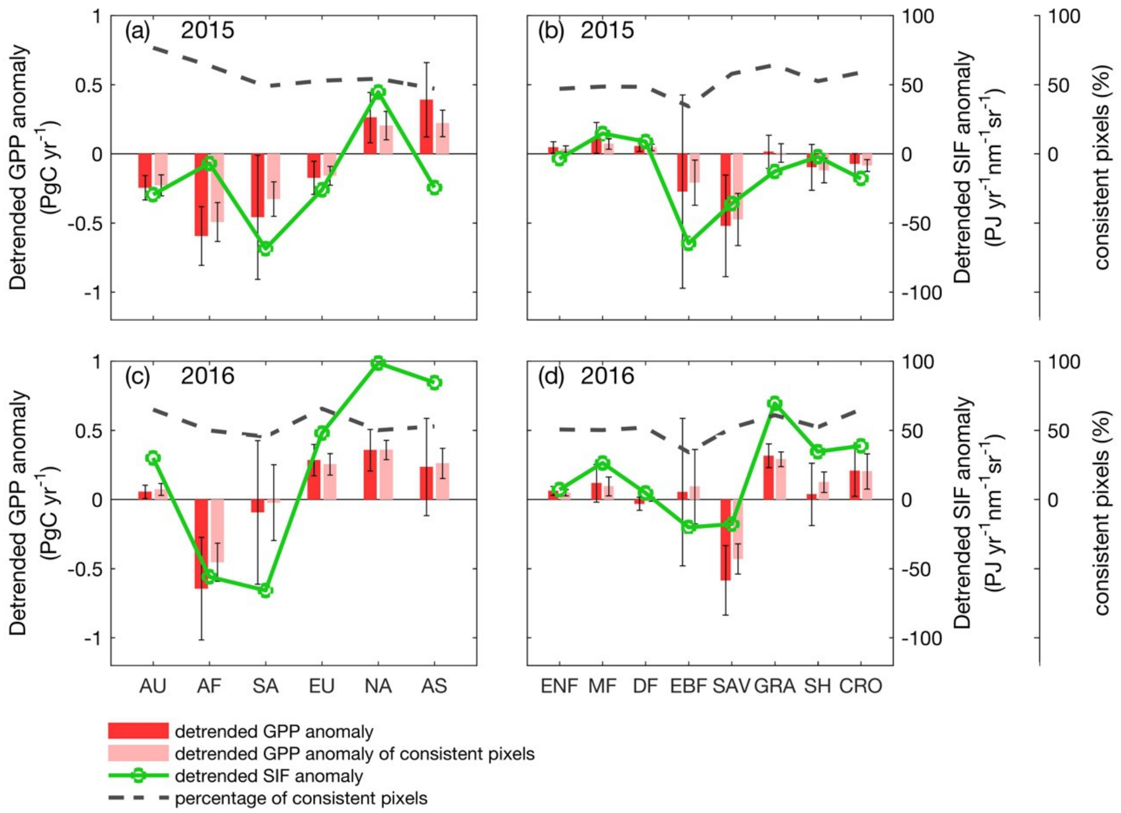

Figure 3. Detrended GPP anomalies (PgC yr^{-1}) and detrended SIF anomalies (PJ yr^{-1}nm^{-1} sr^{-1}) for each continent and PFT in 2015 (a-b) and 2016 (c-d). Dark red bars and whiskers respectively indicate the mean and the standard deviation of detrended GPP anomalies for each region. Light red bars and whiskers respectively indicate the mean and the standard deviation of detrended GPP anomalies of the consistent pixels in each region. Green solid lines represent the detrended anomalies of SIF from GOMEA. Grey dash lines indicate the percentage of pixels showing significant GPP anomalies (student's test $p<0.05$) for each region. Acronyms for continents are SA (South America), AF (Africa), AU (Australia), NA (North America), EU(Europe) and AS (Asia). Acronyms for PFTs are Evergreen needleleaf forests (ENF), mixed forests (MF), deciduous forests (DF), evergreen broadleaf forests (EBF), savannas (SAV), grasslands (GRA), shrublands (SH) and croplands (CRO).

EBF showed the largest uncertainty in estimated GPP and the least percentage of consistent pixels (34%) between the RS models (Figure 4). In contrast, the anomalies from the ensemble of RS models were consistent on over 50% of the area for other PFTs, especially for SAV, GRA and CRO where the consistent percentage was around 60%. Therefore, using the ensemble of RS models is more robust for SAV, GRA and CRO than for EBF. By only considering the consistent pixels, the ensemble means of RS models for each region or PFT showed similar magnitude and direction of anomalies to their counterparts of all pixels, but with substantially smaller uncertainty (Figure 4). It indicates that the influence of inconsistence pixels was muted in our analysis by using ensemble means. In addition, the detrended anomalies of SIF also tracked the ensemble mean of RS models, corroborating the GPP changes identified by the ensemble mean of RS models.

3. Seasonal variation of RS GPP anomalies

The 2015-2016 El Niño lasted 15 months and gradually modulated global climate regimes. The photosynthesis activities of different PFTs were therefore subjected to the developmental stages of El Niño and showed temporally varying anomalies (Figure 3).

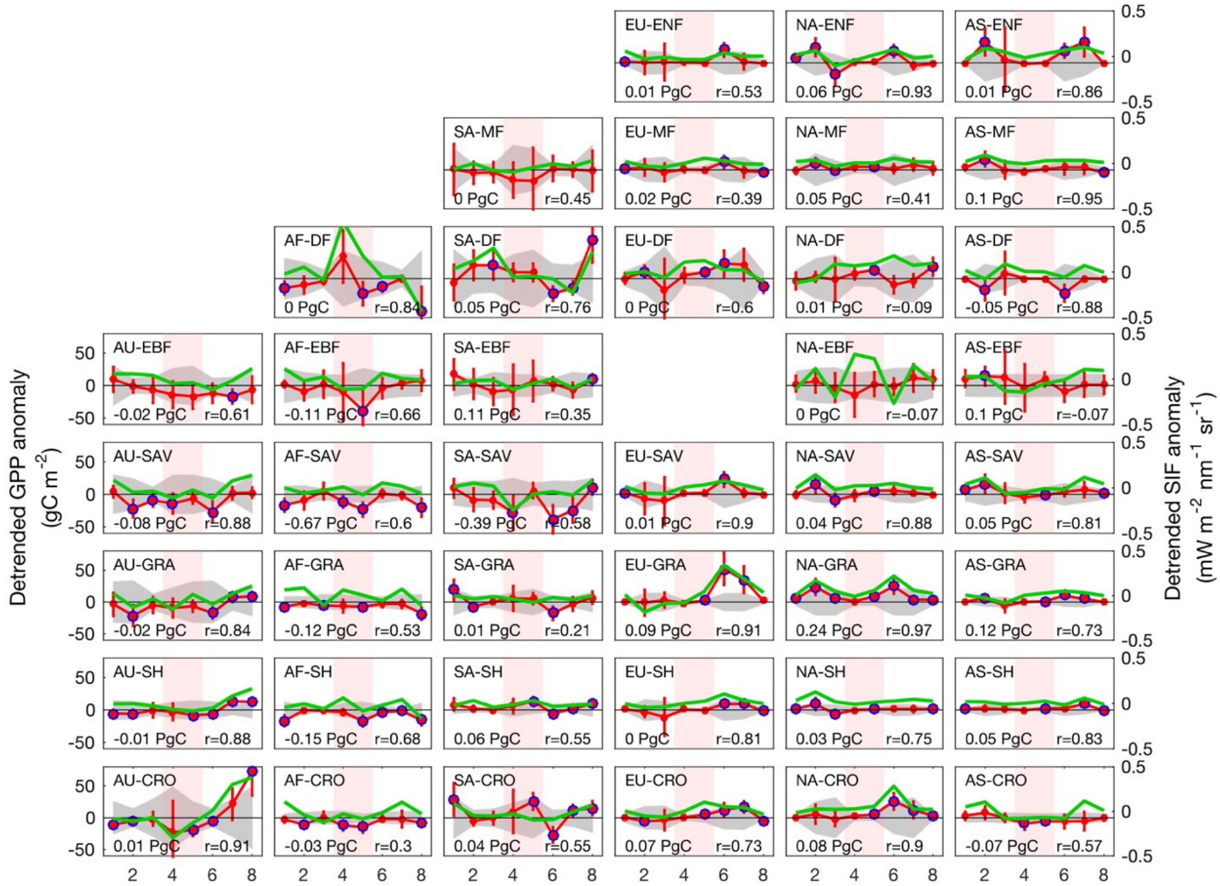

Figure 4. Seasonal variations of detrended GPP anomalies for 8 PFTs (rows) on 6 continents (columns) in 2015-2016, using the linear trends of seasonal RS GPP from 2000 to 2016 as the baselines. Every three months from January 2015 are counted as one season. Red lines and whiskers indicate the average and the standard deviation of RS GPP, respectively. Green lines represent the detrended anomalies of SIF from GOMEA. Blue circles are where the six RS GPP models show coherent GPP anomalies (one-tailed t-test $p < 0.05$). Red shading highlights the peak El Niño period. Grey shading represents the natural variability of GPP, calculated as one standard deviation of detrended GPP anomalies from all RS GPPs for the years 2000-2014. In each panel, the number at the bottom left refers to the total GPP anomaly (unit: PgC) during 2015-2016, the number at the bottom right refers to the correlation coefficient between detrended anomalies of SIF and the ensemble mean of detrended

anomalies of RS GPP (unit: unit less). Acronyms for continents are SA (South America), AF (Africa), AU (Australia), NA (North America), EU(Europe) and AS (Asia).

In the early stage of El Niño (March 2015 to September 2015), we found that SAV and GRA in the Southern Hemisphere showed GPP drops while forests in the Northern Hemisphere demonstrated some increases of GPP (Figure 3). Entering the peak of El Niño (October 2015 to February 2016), more PFTs in the Southern Hemisphere decreased GPP, with EBF and SAV having the largest GPP drops. Meanwhile, the Northern Hemisphere photosynthesis was almost neutral except slight drops from some regions (i.e. CRO in Asia and EBF in North America). After the peak El Niño (February 2016 and after), the Southern Hemisphere photosynthesis gradually recovered to the baseline, except the persisting GPP decreases in SAV and SH. At the same time, the Northern Hemisphere vegetation experienced large GPP increases, spanning most PFTs. Overall, photosynthesis of the Southern Hemisphere decreased during the whole period, primarily contributed by SAV and EBF, while photosynthesis of the Northern Hemisphere increased, mainly before and after the peak of El Niño.

In most regions, GOMEA SIF corroborated the seasonal patterns of RS GPP ensemble mean (Figure 4). The most consistent temporal patterns between SIF and RS GPP ensemble mean were found in SAV (0.79 ± 0.11), SH (0.78 ± 0.11) and ENF (0.77 ± 0.17), and Australia (0.82 ± 0.11), while the least consistent temporal patterns were found in South America (0.51 ± 0.17) and EBF (0.30 ± 0.32).

4. Drivers for the difference between RS GPP

While we used the ensemble mean of RS estimates to detect the impact of El Niño, we noticed that large inter-model variation of GPP products limited the detectability of GPP anomalies at some regions or PFTs (i.e. EBF). Inter-model variation for EBF GPP (18 g C m^{-2} yr^{-1}) was almost the same magnitude as the natural variability of EBF GPP (22 g C m^{-2} yr^{-1}). Our result showed that the large variation in the ensemble was usually driven by some unique simulations from one or two models, such as VPM for EBF and CRO, BEPS for SH and PR for ENF (Figure 5). Models tended to show convergent performance in some regions, particularly in SAV, GRA and Australia. The detrended SIF was not significantly ($p<0.05$) different than the detrended anomalies of most RS models (Figure 5).

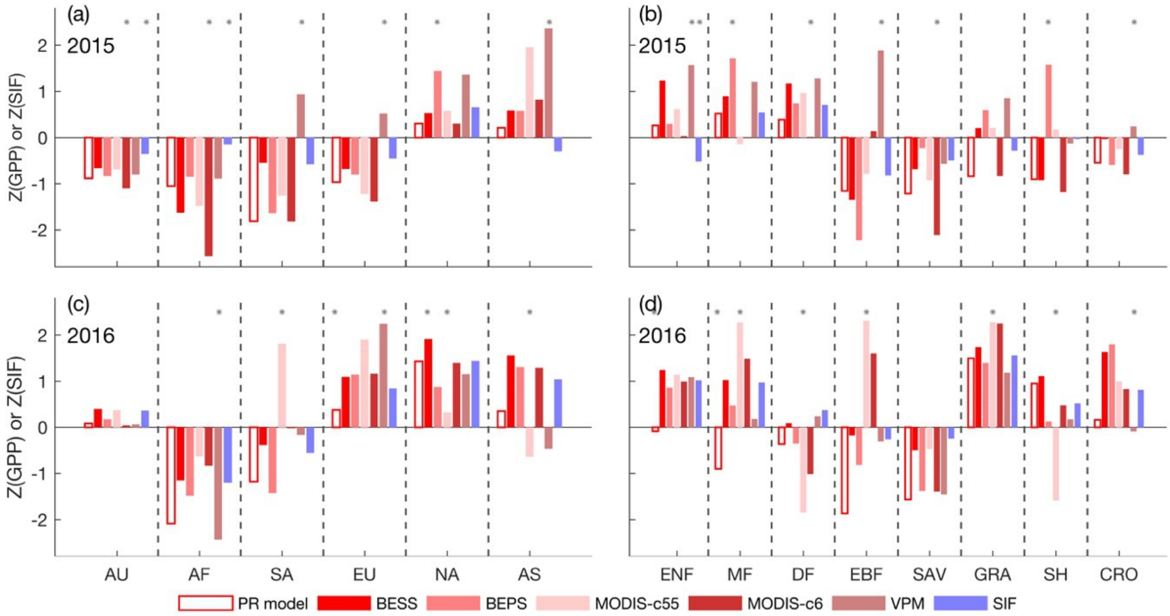

Figure 5. Z scores of the six RS GPP estimates and the GOMEA SIF for each continent and PFT in 2015 (a-b) and 2016 (c-d). "*" indicates that a model is significantly ($p<0.05$) different than others. Acronyms for continents are SA (South America), AF (Africa), AU (Australia), NA (North America), EU(Europe) and AS (Asia). Acronyms for PFTs are Evergreen needleleaf forests (ENF), mixed forests (MF), deciduous forests (DF), evergreen broadleaf forests (EBF), savannas (SAV), grasslands (GRA), shrublands (SH) and croplands (CRO).

The six RS models assessed used different meteorological datasets and RS inputs to simulate GPP, the variations of which can propagate into the inter-model variation of annual GPP (σGPP). We found that σGPP tended to increase with the inter-dataset variations of annual precipitation (σPP; $p<0.01$, $r=0.94$) and annual mean PAR (σPAR; $p<0.05$, $r=0.71$) (Figure 6), suggesting the choices of precipitation and PAR sources contributed to the difference between GPP estimates of different models. Even though precipitation demonstrated the strongest explanatory power for σGPP among all variables, we noticed that only one model (BEPS) in our ensemble explicitly used precipitation as an input. Meanwhile, four members of our ensemble, including MODIS-c55, MODIS-c6, the PR model and BEPS explicitly used vapor pressure deficit (VPD) or relative humidity in the models. However, we found a much weaker correlation between the inter-data variation of VPD (σVPD) and σGPP ($p>0.1$, $r=0.32$) than between σPP and σGPP, suggesting that precipitation impacts GPP not only by VPD but also by other terms related to precipitation (i.e. soil moisture, cloudiness). In addition, we found the choice of vegetation indices for the RS models played a positive but non-significant role in explaining σGPP ($p>0.1$, $r=0.56$), suggesting the different proxies used for fAPAR resulted in smaller changes in GPP than moisture conditions and PAR in the RS models examined.

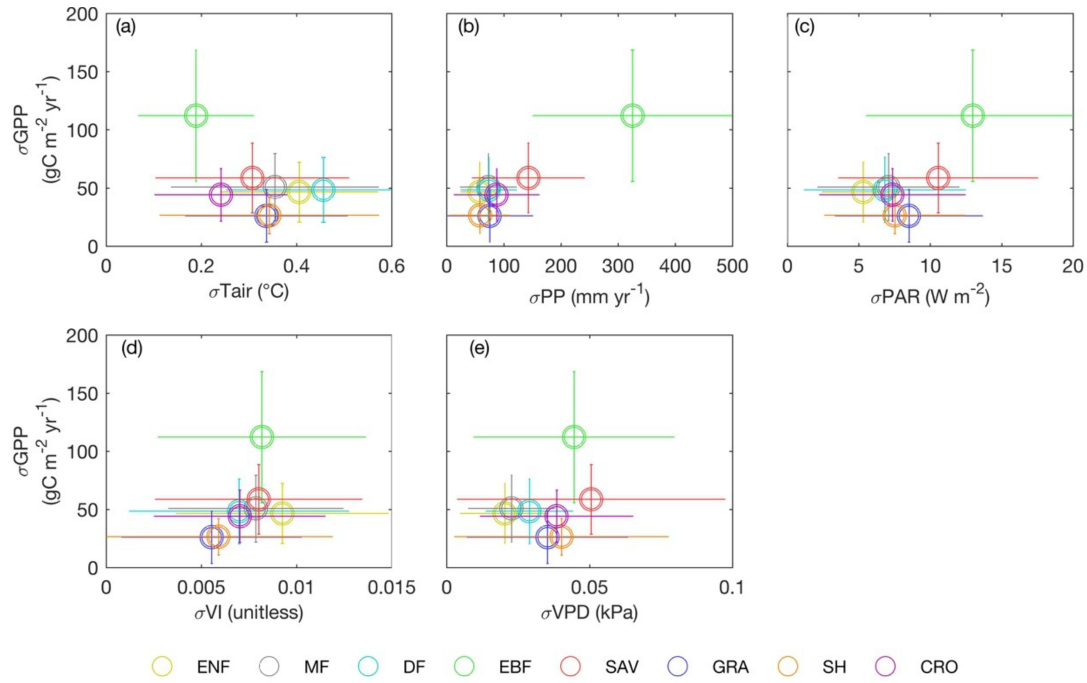

Figure 6. Comparison of the inter-model variation of the annual GPP estimated by the six RS models (σGPP) to the inter-dataset variation of multiple climate datasets used to drive RS GPP models in 2015. (a) σGPP versus the inter-dataset variation of annual mean air temperature (σTair) acquired from CRU, CRU-NCEP, NCEP Reanalysis II, ERAI and MERRA2; (b) σGPP versus the inter-dataset variation of annual precipitation (σPP) acquired from CRU, CRU-NCEP, NCEP Reanalysis II, ERAI, MERRA2 and TRMM; (c) σGPP versus the inter-dataset variation of annual mean PAR (σPAR) acquired from CRU, CRU-NCEP and ERAI; (d) σGPP versus the inter-dataset variation of annual mean vegetation indices (σVI), including MODIS NDVI, MODIS EVI and AVHRR fAPAR. (e) σGPP versus the inter-dataset variation of annual mean vapor pressure deficit (σVPD) acquired from CRU, CRU-NCEP and ERAI. Error bars indicate the spatial variations of investigated variables within each PFT. Acronyms for PFTs are Evergreen needleleaf forests (ENF), mixed forests (MF), deciduous forests (DF), evergreen broadleaf forests (EBF), savannas (SAV), grasslands (GRA), shrublands (SH) and croplands (CRO).

Discussion

El Niño influences the natural variability of the terrestrial carbon sink through modulating global climate regimes. The impact of El Niño on photosynthesis and the contribution of the changing photosynthesis to the known reduction of the terrestrial carbon sink are highly uncertain. Using six RS photosynthesis products and a SIF dataset, this study found that the 2015-2016 El Niño drove a negative GPP anomaly of -0.70 ± 1.20 PgC in 2015 and a slight positive anomaly of 0.05 ± 0.88 PgC in 2016. According to the ensemble mean of RS models, the GPP reduction accounted for 60% of the NEP reduction in 2015, but also implies a dominant role of increasing Reco and potentially wild fires in reducing NEP in 2016 [16,24]. Savannas photosynthesis decreased the most by -1.1 ± 0.52 PgC, followed by a very uncertain GPP reduction of -0.22 ± 0.98 PgC from evergreen broadleaf forests. The

Northern Hemisphere GPP increased before and after the peak El Niño, contributed mostly by grasslands (0.33 ± 0.13 PgC) . RS GPP ensemble showed consistent anomalies over about 60% of savannas, grasslands and croplands regions, but models diverged over key ecoregions like tropical forests. SIF datasets corroborated the temporal patterns of the ensemble mean GPP in most regions except EBF.

Our results show that the RS GPP products unanimously identified a strong reduction of GPP in Africa during the 2015-2016 El Niño. African biomes contributed a negative anomaly of -1.24 ± 0.33 PgC in 2015 and 2016, surpassing the GPP anomalies of other regions. However, this result contradicts a recent study that suggested an increase of respiration and fires drove down NEP in the tropical Africa (15°N-15°S) during the 2015-2016 El Niño, with GPP remained unchanged [24]. Differences in the choice of baselines may explain the contrasting results: in this study, we used the linear trend of 17-year period from 2000 to 2016 as the baseline to calculate the natural variability of GPP; Liu et al. [24] used one year, 2011 (a strong La Niña year), as the baseline to calculate the anomaly of GPP. We also found a limited contribution of African tropical ecosystem GPP when using 2011 as a baseline (Figure 7). By using 2011 as the baseline, the positive impact of the GPP increasing trend can offset the negative impact of El Niño on GPP, and affected the interpretation of El Niño impacts. We suggest that El Niño impact assessment studies should be done using a well-characterized long-term baseline estimate of GPP, instead of one representative year. This result also highlights a large impact of the 2015-2016 El Niño on savanna ecosystems (Figure 3, 4) and echoes the reported dominating role of arid and semi-arid regions in influencing the inter-annual variability of the land carbon sink [13,62].

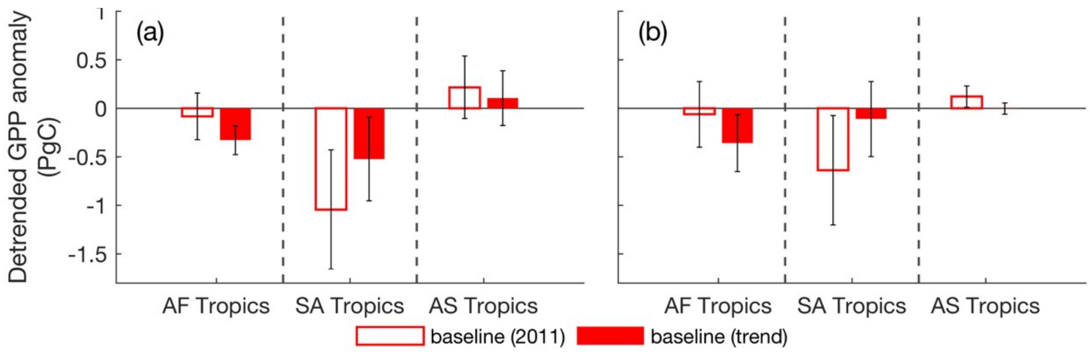

Figure 7. Detrended GPP anomalies (PgC) in tropics (15°N-15°S) in 2015 (a) and 2016 (b), using either a La Niña year (2011) or the long-term trend as the baseline. Acronyms for continents are SA (South America), AF (Africa) and AS (Asia).

Even though our results provided an ensemble mean that can be used to detect regional anomalies of GPP, the large divergence between remote sensing GPP models or between models and SIF over EBF points out the complexity of this PFT. In this study, we found that the divergence between RS GPP models was significantly related to the divergence between precipitation datasets of various sources, as the impact of precipitation on GPP was either explicitly (e.g. BEPS) or implicitly considered in models via VPD (e.g. MODIS), soil moisture (e.g. VPM) or cloudiness (e.g. BESS). Precipitation datasets disagreed the most in the tropics during the 2015-2016 El Niño event (Figure 6, S3), consequently leading to the largest uncertainty of GPP estimates in tropical regions. A recent site-level study [63] and a global-scale study [64] echoed our results by suggesting that the different representation of water stress in seven LUE GPP models explained most of the inter-model variation, whether water stress was represented by VPD, evapotranspiration or a proxy of soil water content in those models. We acknowledge that a comprehensive analysis on σGPP and the inter-dataset variation of climate variables requires a complete archive of original inputs of all models, which was beyond the scope of this study. The incompleteness of the original inputs may affect the σPAR-σGPP and σVPD-σGPP relationships we investigated (Figure 6). Nevertheless, the large σGPP emphasizes the importance of considering an ensemble of multiple RS models in order to account for the inherent uncertainty associated with individual model projections. We also suggest further studies test whether members of the ensemble provide equally valid estimates, as we found several models differed significantly (i.e. the VPM model in EBF; Figure 5). The difference between the model abilities emphasizes the need for a better proxy for an ensemble than the simple arithmetic mean.

In addition, we found SIF was only weakly correlated with the ensemble mean of GPP in EBF (Figure 4), which seems consistent with a recent study reporting a decoupling of decreasing SIF and increasing NDVI over the Amazon rainforest [36]. However, several results of this study project doubts on the so-called decoupling issue. First, the weak correlation between SIF and ensemble mean GPP was likely caused by the unique performances of just one or two models, while the GPP anomalies of most models actually varied in the same direction of SIF anomalies (Figure 5). Secondly, after removing the long-term trend of vegetation indices (VIs; i.e. NDVI, EVI and fAPAR), we found the anomalies of VIs were actually negative in tropics in 2015 and 2016 (Figure S3), in contrast to what was previously reported [36]. The degradation of GOMEA SIF may also confound the anomalies of SIF detected [37], but we found the negative anomalies of GOMEA SIF persisted even after we removed the artefact (Figure 5). Overall, we found SIF, VIs and GPP estimates in most cases demonstrated negative anomalies in tropics, calling into questions a decoupling of SIF and GPP or decoupling of SIF and VIs. We acknowledge that our method to remove the artefact of SIF, though statistically robust (Figure S4), is not a complete solution to filter noise and degradation of SIF signals. Further studies on the processing pipeline of SIF data [65] and the mechanisms underlying SIF [66] are essential to our correct interpretation of the relationship between SIF and GPP.

Conclusions

The 2015-2016 El Niño is one of the strongest El Niño events in the modern record, rivalling the magnitude of the large 1997-1998 event [16,38]. It provides a unique chance to study the impact of El

Niño on the terrestrial carbon sink in the satellite-era. Using six RS GPP products and the GOME-2 SIF dataset, we assessed the response of global photosynthesis to the 2015-2016 El Niño, as well as the spatial and temporal variations of the response.

At the global scale, our results show that global photosynthesis decreased by 0.70 ± 1.20 PgC in 2015 based on an ensemble of six RS models. The decrease in GPP accounted for 60% of the NEP reduction. In 2016, however, GPP demonstrated a slight positive detrended anomaly of 0.05 ± 0.88, which implies that the large reduction in the terrestrial carbon sink in 2016 was likely due to increased respiration and biomass burning.

At the regional scale, the ensemble of RS GPP products identified significant GPP changes over 50% of the vegetated land surface. All RS GPP products found that savanna ecosystems decreased photosynthesis severely in response to El Niño, followed by evergreen broadleaf forests. The Northern Hemisphere GPP increased before and after the peak El Niño period, especially for grasslands. Despite the consistency for many regions, tropical rainforests estimates showed large variations between the ensemble members, likely driven by discrepancies between the moisture forcings for models. The temporal patterns of SIF and the RS GPP ensemble mean agreed well except in EBF. Further research on the consistency and inconsistency between various RS GPP products, on the relationships between SIF and different RS GPP, and on techniques for estimating tropical forest photosynthesis from space, is needed to reduce the uncertainty associated with global GPP products reported here.

Additional Information

Acknowledgments
XL and TFK would like to thank Dr. Qing Zhu from the Lawrence Berkeley National Laboratory for providing the CRU-NCEP data. JBF carried out research at the Jet Propulsion Laboratory, California Institute of Technology, under a contract with the National Aeronautics and Space Administration. California Institute of Technology. Government sponsorship acknowledged. Copyright 2018. All rights reserved.

Data Accessibility
Data used in study are available per request to the corresponding authors.

Authors' Contributions
XL and TFK designed the study. XL performed the analysis and wrote the first draft, with input from TFK. TFK, JF, JJ, JMC, CJ, WJ, NP, YR and JT provided data for the analysis. All authors discussed and commented on the writing.

Competing Interests
We have no competing interests.

Funding
XL, TFK, and JBF were supported by the NASA Terrestrial Ecology Program IDS Award NNH17AE86I. TFK acknowledges additional support from the Director, Office of Science, Office of Biological and Environmental Research of the US Department of Energy under Contract DE-AC02-05CH11231 as part of the Rubisco SFA. The BESS product was funded by National Research Foundation of Korea (NRF-2014R1A2A1A11051134).

Supplementary Information

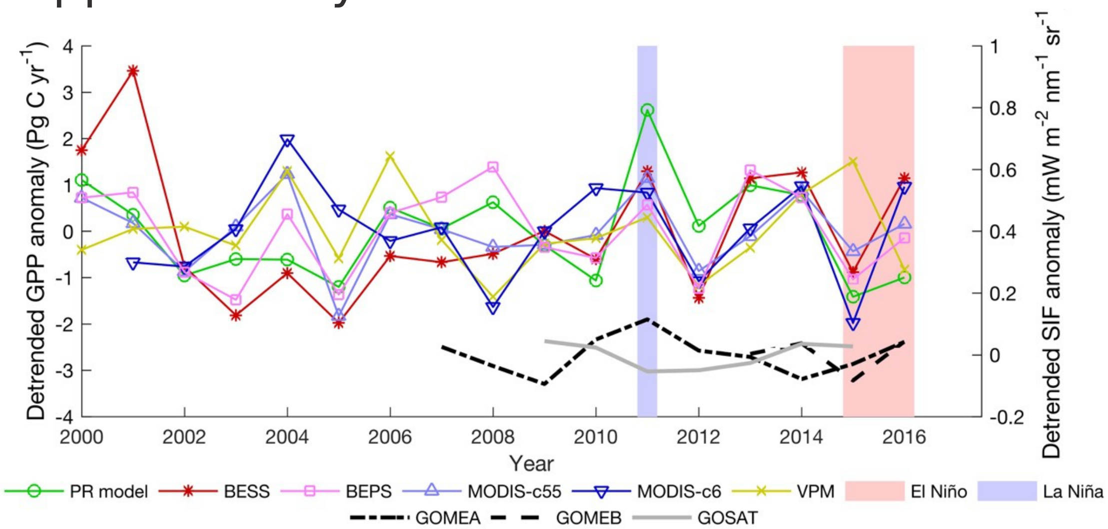

Figure S1. The detrended RS GPP and SIF anomalies from 2000 to 2016, using the detrended time-average GPP(SIF) of the same period as the baseline.

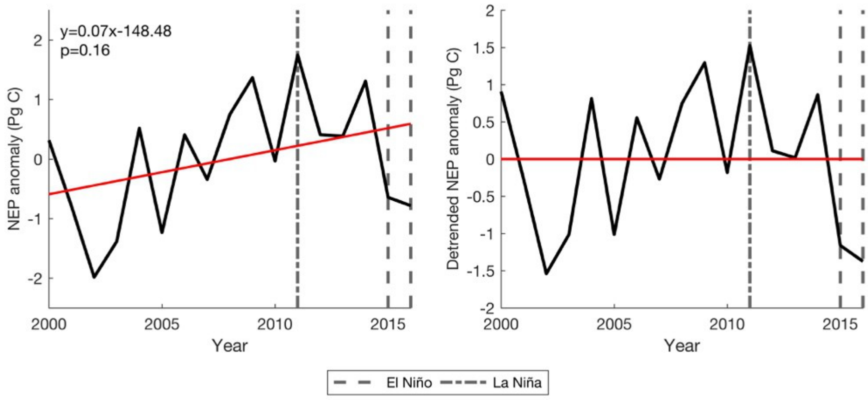

Figure S2. The NEP anomalies and the detrended NEP anomalies from 2000 to 2016. NEP is calculated as the net residual land CO_2 sink, estimated by the Global Carbon Project (GCP).

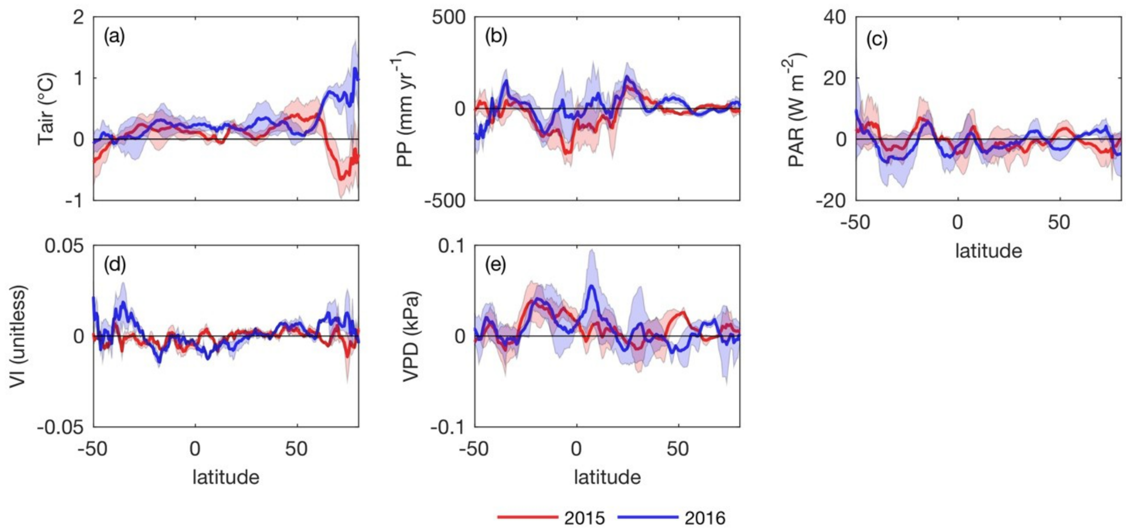

Figure S3. Latitudinal distribution of ensembles of air temperature (Tair), precipitation (PP), photosynthetic active radiation (PAR), vegetation indices (VI) and vapor pressure deficit (VPD) in 2015 and 2016, using the linear trends of variables from 2000 to 2016 as the baselines. The ensemble of Tair is consisted of CRU, CRU-NCEP, NCEP Reanalysis II, ERAI and MERRA2; the ensemble of PP is consisted of CRU, CRU-NCEP, NCEP Reanalysis II, ERAI, MERRA2 and TRMM; the ensemble of PAR is consisted of CRU, CRU-NCEP and ERAI; the ensemble of VI is consisted of MODIS NDVI, MODIS EVI (only 2015) and AVHRR fAPAR; the ensemble of VPD is consisted of CRU, CRU-NCEP and ERAI. The shadings indicate the inter-dataset variations of each variable.

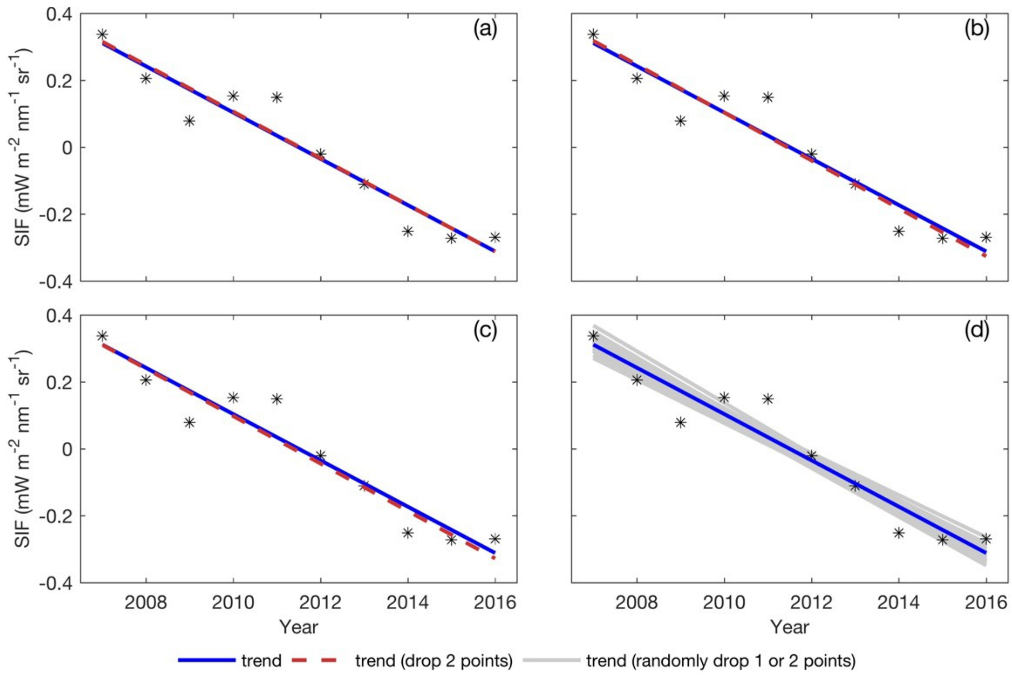

Figure S4. Uncertainty of GOMEA SIF trend. Blue line is the baseline of GOMEA SIF we used in this study. (a) first two data points were dropped to fit the line; (b) the last two data points were dropped to fit the line; (c) the first and the last data points were dropped to fit the line; (d) One or two data points were randomly dropped in 400 tests to fit the line. In 98.3% of the tests there was a negative detrended SIF anomaly in 2015 and a positive detrended SIF anomaly in 2016.

References

1. Le Quéré C *et al.* 2017 Global Carbon Budget 2017. *Earth Syst. Sci. Data Discuss.* , 1–79. (doi:10.5194/essd-2017-123)
2. Ballantyne AP, Alden CB, Miller JB, Trans PP, White JWC. 2012 Increase in observed net carbon dioxide uptake by land and oceans during the past 50 years. *Nature* **488**, 70–73. (doi:10.1038/nature11299)
3. Baker TR *et al.* 2004 Increasing biomass in Amazonian forest plots. *Philos. Trans. R. Soc. B Biol. Sci.* **359**, 353–365. (doi:10.1098/rstb.2003.1422)
4. Lewis SL *et al.* 2009 Increasing carbon storage in intact African tropical forests. *Nature* **457**, 1003–1006. (doi:10.1038/nature07771)
5. Zhu Z *et al.* 2016 Greening of the Earth and its drivers. *Nat. Clim. Chang.* **6**, 791–795. (doi:10.1038/nclimate3004)
6. Los SO. 2013 Analysis of trends in fused AVHRR and MODIS NDVI data for 1982-2006: Indication for a CO2 fertilization effect in global vegetation. *Global Biogeochem. Cycles* **27**, 318–330. (doi:10.1002/gbc.20027)
7. Keenan TF, Prentice IC, Canadell JG, Williams CA, Wang H, Raupach M, Collatz GJ. 2016 Recent pause in the growth rate of atmospheric CO2 due to enhanced terrestrial carbon uptake. *Nat. Commun.* **7**, 13428. (doi:10.1038/ncomms13428)
8. Schimel D, Stephens BB, Fisher JB. 2015 Effect of increasing CO_2 on the terrestrial carbon cycle. *Proc. Natl. Acad. Sci.* **112**, 436–441. (doi:10.1073/pnas.1407302112)
9. Keenan TF *et al.* 2014 Net carbon uptake has increased through warming-induced changes in temperate forest phenology. *Nat. Clim. Chang.* **4**, 598–604. (doi:10.1038/nclimate2253)
10. Keenan TF *et al.* 2012 Terrestrial biosphere model performance for inter-annual variability of land-atmosphere CO 2 exchange. *Glob. Chang. Biol.* **18**, 1971–1987. (doi:10.1111/j.1365-2486.2012.02678.x)
11. Zeng N, Mariotti A, Wetzel P. 2005 Terrestrial mechanisms of interannual CO2 variability. *Global Biogeochem. Cycles* **19**, 1–15. (doi:10.1029/2004GB002273)
12. Cox PM, Pearson D, Booth BB, Friedlingstein P, Huntingford C, Jones CD, Luke CM. 2013 Sensitivity of tropical carbon to climate change constrained by carbon dioxide variability. *Nature* **494**, 341–344. (doi:10.1038/nature11882)
13. Ahlström A *et al.* 2015 The dominant role of semi-arid ecosystems in the trend and variability of the land CO_2 sink. *Science (80-.).* **348**, 895 LP-899.
14. Wang W *et al.* 2013 Variations in atmospheric CO2 growth rates coupled with tropical temperature. *Proc. Natl. Acad. Sci.* **110**, 13061–13066. (doi:10.1073/pnas.1219683110)
15. Schwalm CR *et al.* 2012 Reduction in carbon uptake during turn of the century drought in western North America. *Nat. Geosci.* **5**, 551–556. (doi:10.1038/ngeo1529)
16. Chen Y, Morton DC, Andela N, van der Werf GR, Giglio L, Randerson JT. 2017 A pan-tropical cascade of fire driven by El Niño/Southern Oscillation. *Nat. Clim. Chang.* **7**, 906–911. (doi:10.1038/s41558-017-0014-8)
17. Qie L *et al.* 2017 Long-term carbon sink in Borneo’s forests halted by drought and vulnerable to edge effects. *Nat. Commun.* **8**, 1966. (doi:10.1038/s41467-017-01997-0)
18. Zhu Z, Piao S, Xu Y, Bastos A, Ciais P, Peng S. 2017 The effects of teleconnections on carbon fluxes of global terrestrial ecosystems. *Geophys. Res. Lett.* **44**, 3209–3218. (doi:10.1002/2016GL071743)
19. Gonsamo A, Chen JM, Lombardozzi D. 2016 Global vegetation productivity response to climatic oscillations during the satellite era. *Glob. Chang. Biol.* **22**, 3414–3426. (doi:10.1111/gcb.13258)
20. Allakhverdiev SI, Kreslavski VD, Klimov V V., Los DA, Carpentier R, Mohanty P. 2008 Heat stress: An overview of molecular responses in photosynthesis. *Photosynth. Res.* **98**, 541–550. (doi:10.1007/s11120-008-9331-0)
21. Bond-Lamberty B, Thomson A. 2010 Temperature-associated increases in the global soil respiration record. *Nature* **464**, 579–582. (doi:10.1038/nature08930)
22. Wang X *et al.* 2014 A two-fold increase of carbon cycle sensitivity to tropical temperature variations. *Nature* **506**, 212–215. (doi:10.1038/nature12915)
23. Jung M *et al.* 2017 Compensatory water effects link yearly global land CO 2 sink changes to temperature. *Nature* **541**, 516–520. (doi:10.1038/nature20780)
24. Liu J *et al.* 2017 Contrasting carbon cycle responses of the tropical continents to the 2015–2016 El Niño. *Science (80-.).* **358**. (doi:10.1126/science.aam5690)
25. Jones CD, Collins M, Cox PM, Spall SA. 2001 The carbon cycle response to ENSO: A coupled climate-carbon cycle model study. *J. Clim.* **14**, 4113–4129. (doi:10.1175/1520-0442(2001)014<4113:TCCRTE>2.0.CO;2)
26. Cavaleri MA, Coble AP, Ryan MG, Bauerle WL, Loescher HW, Oberbauer SF. 2017 Tropical rainforest carbon sink declines during El Niño as a result of reduced photosynthesis and increased respiration rates. *New Phytol.* (doi:10.1111/nph.14724)
27. Qian H, Joseph R, Zeng N. 2008 Response of the terrestrial carbon cycle to the El Ni˜no-Southern Oscillation. *Tellus B Chem. Phys. Meteorol.* **60**, 537–550. (doi:10.1111/j.1600-0889.2008.00360.x)
28. Wang J, Zeng N, Wang M, Jiang F, Wang H, Jiang Z. 2017 Contrasting terrestrial carbon cycle responses to the two strongest El Niño events: 1997–98 and 2015–16 El Niños. *Earth Syst. Dyn. Discuss.* , 1–32. (doi:10.5194/esd-2017-46)
29. Zhao M, Heinsch FA, Nemani RR, Running SW. 2005 Improvements of the MODIS terrestrial gross and net primary production global data set. *Remote Sens. Environ.* **95**, 164–176. (doi:10.1016/j.rse.2004.12.011)
30. Xiao J *et al.* 2010 A continuous measure of gross primary production for the conterminous United States derived from MODIS and AmeriFlux data. *Remote Sens. Environ.* **114**, 576–591. (doi:10.1016/j.rse.2009.10.013)
31. Hashimoto H, Nemani RR, White MA, Jolly WM, Piper SC, Keeling CD, Myneni RB, Running SW. 2004 El Niño-Southern Oscillation-induced variability in terrestrial carbon cycling. *J. Geophys. Res. D Atmos.* **109**, 1–8. (doi:10.1029/2004JD004959)
32. Ballantyne A *et al.* 2017 Accelerating net terrestrial carbon uptake during the warming hiatus due to reduced respiration. *Nat. Clim. Chang.* **7**, 148–152. (doi:10.1038/nclimate3204)
33. Porcar-Castell A, Tyystjärvi E, Atherton J, Van Der Tol C, Flexas J, Pfündel EE, Moreno J, Frankenberg C, Berry JA. 2014 Linking chlorophyll a fluorescence to photosynthesis for remote sensing applications: Mechanisms and challenges. *J. Exp. Bot.* **65**, 4065–4095. (doi:10.1093/jxb/eru191)
34. Frankenberg C *et al.* 2011 New global observations of the terrestrial carbon cycle from GOSAT : Patterns of plant fluorescence with gross primary productivity. **38**, 1–6. (doi:10.1029/2011GL048738)
35. Guanter L, Frankenberg C, Dudhia A, Lewis PE, Gómez-Dans J, Kuze A, Suto H, Grainger RG. 2012 Retrieval and global assessment of terrestrial chlorophyll fluorescence from GOSAT space measurements. *Remote Sens. Environ.* **121**, 236–251. (doi:10.1016/j.rse.2012.02.006)
36. Yang J, Tian H, Pan S, Chen G, Zhang B, Dangal S. 2018 Amazon droughts and forest responses: Largely

reduced forest photosynthesis but slightly increased canopy greenness during the extreme drought of 2015/2016. *Glob. Chang. Biol.* (doi:10.1111/gcb.14056)

37. Zhang Y, Joiner J, Gentine P, Zhou S. 2018 Reduced solar-induced chlorophyll fluorescence from GOME-2 during Amazon drought caused by dataset artifacts. *Glob. Chang. Biol.* (doi:10.1111/gcb.14134)
38. Jiménez-Muñoz JC, Mattar C, Barichivich J, Santamaría-Artigas A, Takahashi K, Malhi Y, Sobrino JA, Schrier G Van Der. 2016 Record-breaking warming and extreme drought in the Amazon rainforest during the course of El Niño 2015-2016. *Sci. Rep.* **6**, 1–7. (doi:10.1038/srep33130)
39. Panisset JS, Libonati R, Gouveia CMP, Machado-Silva F, França DA, França JRA, Peres LF. 2017 Contrasting patterns of the extreme drought episodes of 2005, 2010 and 2015 in the Amazon Basin. *Int. J. Climatol.* (doi:10.1002/joc.5224)
40. Chatterjee A *et al.* 2017 Influence of El Niño on atmospheric CO2over the tropical Pacific Ocean: Findings from NASA's OCO-2 mission. *Science (80-.).* **358**. (doi:10.1126/science.aam5776)
41. Monteith JL. 1972 Solar Radiation and Productivity in Tropical Ecosystems. *J. Appl. Ecol.* **9**, 747–766.
42. Monteith JL. 1977 Climate and the Efficiency of Crop Production in Britain [and Discussion]. *Philos. Trans. R. Soc. B Biol. Sci.* **281**, 277–294. (doi:10.1098/rstb.1977.0140)
43. Running SW, Nemani RR, Heinsch FA, Zhao M, Reeves M, Hashimoto H. 2004 A Continuous Satellite-Derived Measure of Global Terrestrial Primary Production. *Bioscience* **54**, 547. (doi:10.1641/0006-3568(2004)054[0547:ACSMOG]2.0.CO;2)
44. Zhang Y, Xiao X, Wu X, Zhou S, Zhang G, Qin Y, Dong J. 2017 A global moderate resolution dataset of gross primary production of vegetation for 2000–2016. *Sci. Data* **4**, 170165. (doi:10.1038/sdata.2017.165)
45. De Kauwe MG, Keenan TF, Medlyn BE, Prentice IC, Terrer C. 2016 Satellite based estimates underestimate the effect of CO2 fertilization on net primary productivity. *Nat. Clim. Chang.* **6**, 892–893. (doi:10.1038/nclimate3105)
46. Xiao X, Hollinger D, Aber J, Goltz M, Davidson EA, Zhang Q, Moore B. 2004 Satellite-based modeling of gross primary production in an evergreen needleleaf forest. *Remote Sens. Environ.* **89**, 519–534. (doi:10.1016/j.rse.2003.11.008)
47. Xiao X, Boles S, Frolking S, Salas W, Moore I, Li C, He L, Zhao R. 2002 Observation of flooding and rice transplanting of paddy rice fields at the site to landscape scales in China using VEGETATION sensor data. *Int. J. Remote Sens.* **23**, 3009–3022. (doi:10.1080/01431160110107734)
48. Farquhar GD, von Caemmerer S, Berry JA. 1980 A biochemical model of photosynthetic CO2 assimilation in leaves of C 3 species. *Planta* **149**, 78–90. (doi:10.1007/BF00386231)
49. Ryu Y *et al.* 2011 Integration of MODIS land and atmosphere products with a coupled-process model to estimate gross primary productivity and evapotranspiration from 1 km to global scales. *Global Biogeochem. Cycles* **25**, GB4017. (doi:10.1029/2011GB004053)
50. Jiang C, Ryu Y. 2016 Multi-scale evaluation of global gross primary productivity and evapotranspiration products derived from Breathing Earth System Simulator (BESS). *Remote Sens. Environ.* **186**, 528–547. (doi:10.1016/j.rse.2016.08.030)
51. Ryu Y *et al.* 2012 On the temporal upscaling of evapotranspiration from instantaneous remote sensing measurements to 8-day mean daily-sums. *Agric. For. Meteorol.* **152**, 212–222. (doi:10.1016/j.agrformet.2011.09.010)
52. Prentice IC, Dong N, Gleason SM, Maire V, Wright IJ. 2014 Balancing the costs of carbon gain and water transport: Testing a new theoretical framework for plant functional ecology. *Ecol. Lett.* **17**, 82–91. (doi:10.1111/ele.12211)
53. Wang H, Prentice IC, Keenan TF, Davis TW, Wright IJ, Cornwell WK, Evans BJ, Peng C. 2017 Towards a universal model for carbon dioxide uptake by plants. *Nat. Plants* **3**, 734–741. (doi:10.1038/s41477-017-0006-8)
54. Zhu Z *et al.* 2013 Global data sets of vegetation leaf area index (LAI)3g and fraction of photosynthetically active radiation (FPAR)3g derived from global inventory modeling and mapping studies (GIMMS) normalized difference vegetation index (NDVI3G) for the period 1981 to 2. *Remote Sens.* **5**, 927–948. (doi:10.3390/rs5020927)
55. Harris I, Jones PD, Osborn TJ, Lister DH. 2014 Updated high-resolution grids of monthly climatic observations - the CRU TS3.10 Dataset. *Int. J. Climatol.* **34**, 623–642. (doi:10.1002/joc.3711)
56. Chen J., Liu J, Cihlar J, Goulden M. 1999 Daily canopy photosynthesis model through temporal and spatial scaling for remote sensing applications. *Ecol. Modell.* **124**, 99–119. (doi:10.1016/S0304-3800(99)00156-8)
57. He L, Chen JM, Gonsamo A, Luo X, Wang R, Liu Y, Liu R. 2018 Changes in the Shadow: The Shifting Role of Shaded Leaves in Global Carbon and Water Cycles Under Climate Change. *Geophys. Res. Lett.* **82**, 387. (doi:10.1029/2018GL077560)
58. Luo X *et al.* 2018 Comparison of Big-Leaf, Two-Big-Leaf, and Two-Leaf Upscaling Schemes for Evapotranspiration Estimation Using Coupled Carbon-Water Modeling. *J. Geophys. Res. Biogeosciences* **123**. (doi:10.1002/2017JG003978)
59. Friedl MA, Sulla-Menashe D, Tan B, Schneider A, Ramankutty N, Sibley A, Huang X. 2010 MODIS Collection 5 global land cover: Algorithm refinements and characterization of new datasets. *Remote Sens. Environ.* **114**, 168–182. (doi:10.1016/j.rse.2009.08.016)
60. Joiner J, Yoshida Y, Guanter L, Middleton EM. 2016 New methods for the retrieval of chlorophyll red fluorescence from hyperspectral satellite instruments: Simulations and application to GOME-2 and SCIAMACHY. *Atmos. Meas. Tech.* **9**, 3939–3967. (doi:10.5194/amt-9-3939-2016)
61. Shapiro SS, Wilk MB. 1965 An Analysis of Variance Test for Normality (Complete Samples). *Biometrika* **52**, 591–611.
62. Poulter B *et al.* 2014 Contribution of semi-arid ecosystems to interannual variability of the global carbon cycle. *Nature* **509**, 600–603. (doi:10.1038/nature13376)
63. Yuan W *et al.* 2014 Global comparison of light use efficiency models for simulating terrestrial vegetation gross primary production based on the LaThuile database. *Agric. For. Meteorol.* **192–193**, 108–120. (doi:10.1016/j.agrformet.2014.03.007)
64. Cai W, Yuan W, Liang S, Liu S, Dong W, Chen Y, Liu D, Zhang H. 2014 Large differences in terrestrial vegetation production derived from satellite-based light use efficiency models. *Remote Sens.* **6**, 8945–8965. (doi:10.3390/rs6098945)
65. Sanders AFJ, Verstraeten WW, Kooreman ML, van Leth TC, Beringer J, Joiner J. 2016 Spaceborne sun-induced vegetation fluorescence time series from 2007 to 2015 evaluated with Australian flux tower measurements. *Remote Sens.* **8**, 1–24. (doi:10.3390/rs8110895)
66. Yang K *et al.* 2018 Sun-induced chlorophyll fluorescence is more strongly related to absorbed light than to

photosynthesis at half-hourly resolution in a rice paddy. *Remote Sens. Environ.* **216**, 658–673. (doi:10.1016/J.RSE.2018.07.008)